nature photonics

Article

https://doi.org/10.1038/s41566-023-01263-4

Single-molecule mid-infrared spectroscopy and detection through vibrationally assisted luminescence

In the format provided by the authors and unedited

Contents

Figure S1: MIR vibrationally-assisted luminescence in additional samples (MIR-VAL).
Figure S2: Fourier transform infrared (FTIR) spectroscopy of individual MSoF cavities.
Section S1: Need for metal nanogaps.
Figure S3: 3D full-wave simulations of NPoF and MSoF cavities.
Figure S4: Effect of microsphere faceting in MSoF cavities.
Figure S5: MIR-VAL correlated to plasmon resonance peak.
Figure S6: Spectral wandering of aS-PL.
Figure S7: Estimating the effect of temperature on MIR-VAL.
Figure S8: Detecting MIR-VAL in rhodamine B (RhB) molecules.
Figure S9: MIR spectrally-tuned vibrationally-assisted luminescence for RhB.
Figure S10: Influence of local optical E field under nanocavity.
Figure S11: Temporal and spatial coherence of MIR-VAL.
Figure S12: Single-molecule dynamics of MIR-VAL signal.
Figure S13: Single-molecule MIR-VAL spectroscopy.
Figure S14: Modulation of PL outside the nanocavity systems.
Section S2: Rate Equation Model.
Figure S15: Temporal dynamics of MIR-VAL.
Section S3: Measurement of MIR-VAL efficiency.

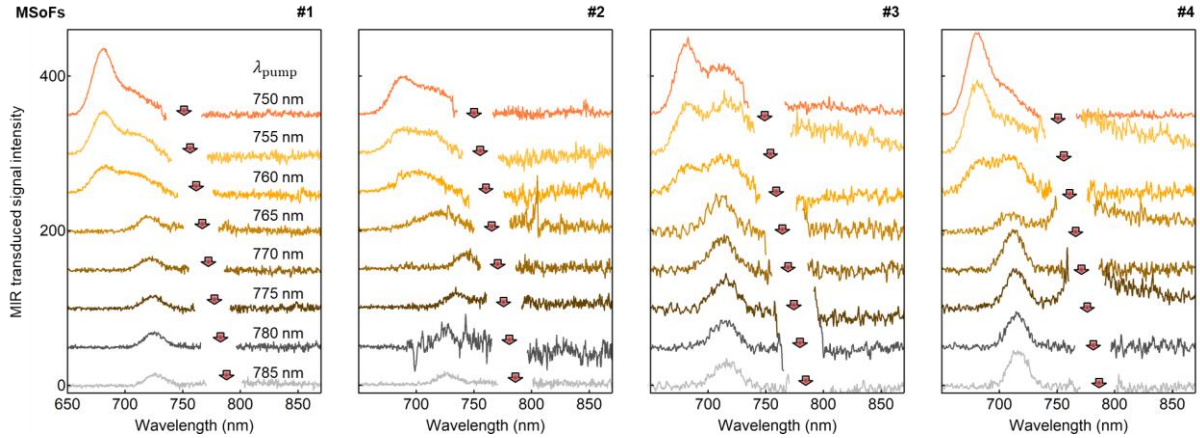

Figure S1: MIR vibrationally-assisted luminescence (MIR-VAL) in additional samples. (**a**) Pump wavelength dependent MIR-VAL for CB-MB system in four different microsphere-on-foil (MSoF) cavities.

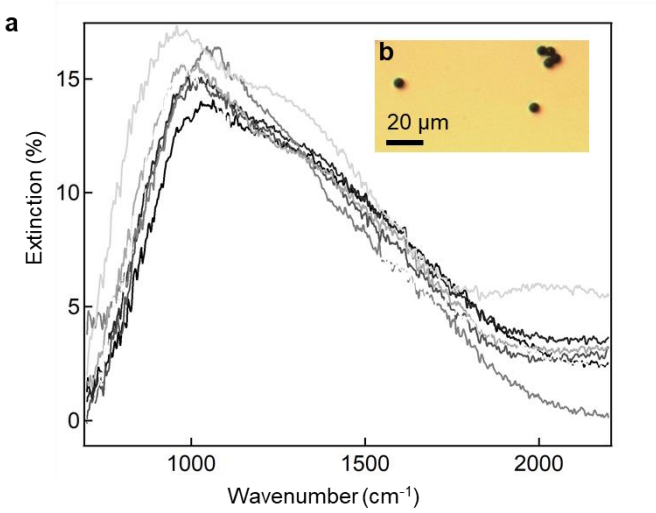

Figure S2: Fourier transform infrared (FTIR) spectroscopy of individual MSoF cavities. (**a**) Mid-infrared extinction spectra obtained for different MSoF cavities. (**b**) Bright field optical image of several isolated MSoF constructs.

Section S1: Need for metal nanogaps:

The presence of metal close to light-emitting molecules is known to suppress the quantum efficiency of the emission and so rightly the referees ask about the need for our metal nanocavity. However, the metal-induced quenching process is suppressed in our sub-nm metal gaps. It is important to note that there are three different process at work in MIR-VAL:

(i) MIR absorption in molecular bonds: Free-space coupling of light to molecular vibrations is extremely weak, as the dipole strength of bond vibrations is <0.1D. The MSoF cavity massively enhances the cross-section. The simulations (Fig.S3) show this enhancement for different nanoparticle sizes. It thus allows coupling of light to only 1-100 molecules placed in the MSoF gaps.

(ii) NIR pumping: The NIR pump drives the vibrationally excited molecule into an electronically excited state. This process is reasonably efficient and fast, as dye molecules have stronger NIR dipoles (~3.8D). However even here the plasmonic cavities greatly boost the overlap of MIR and NIR light by confining the fields in the same nanogaps. Without this dual resonant character, the MIR-VAL process is hundreds of times weaker (as seen comparing the NPoF and MSoF signals).

(iii) Anti-Stokes photoluminescence: Light emission from excited states is sped-up by the Purcell factor (Fig.S3c,e). The calculated radiative Purcell factor in these cavities in these systems is >10^4. Although metal absorption limits the quantum efficiency, it exceeds 40% in the NIR regime because emission is so fast. The MIR-VAL process is thus <10ps compared to ns free-space dye lifetimes.

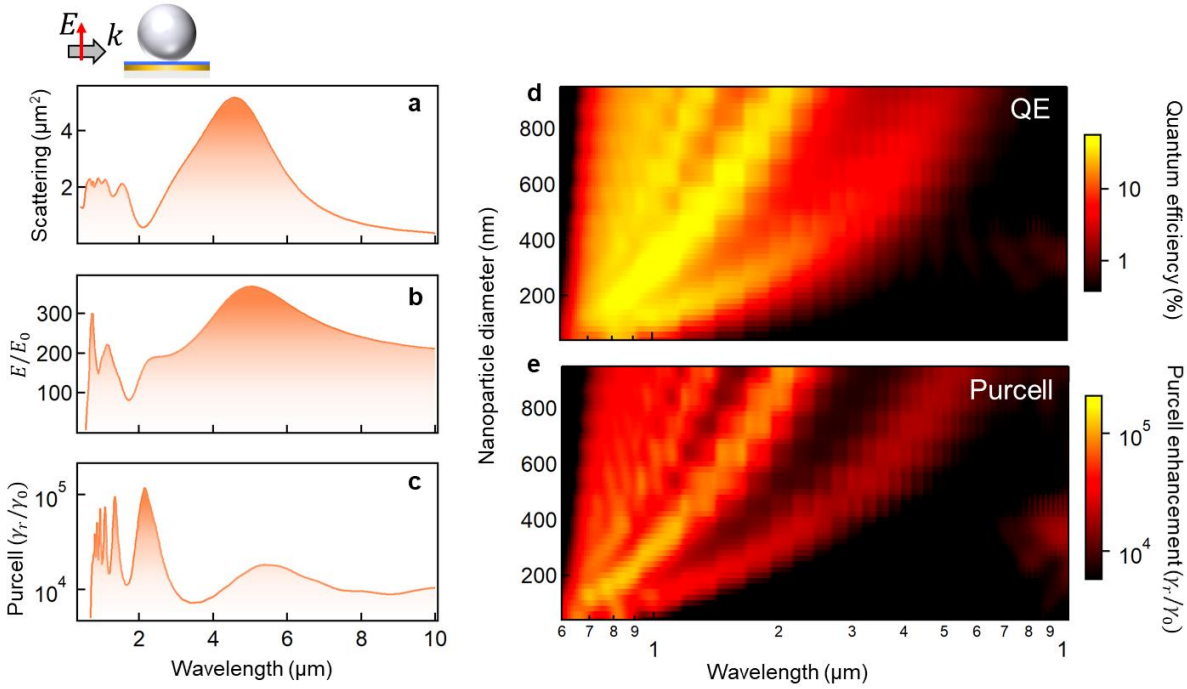

Figure S3: 3D full-wave simulations of NPoF and MSoF cavities. (**a-c**) Calculations for MSoF cavities with sphere diameter of 1um. (**a**) Wavelength dependent scattering cross-section obtained from plane wave illumination with polarization perpendicular to the foil, as shown in the schematic above. (**b**) Near-field enhancement extracted from the center and middle nanogap. (**c**) Calculated enhancement in the radiative Purcell of a dipole placed at the center and middle nanogap. (**d-e**) Quantum efficiency and radiative Purcell enhancement of the light emission from dipole the placed at the center and middle nanogap for various nanoparticle size keeping the gap size of 1nm.

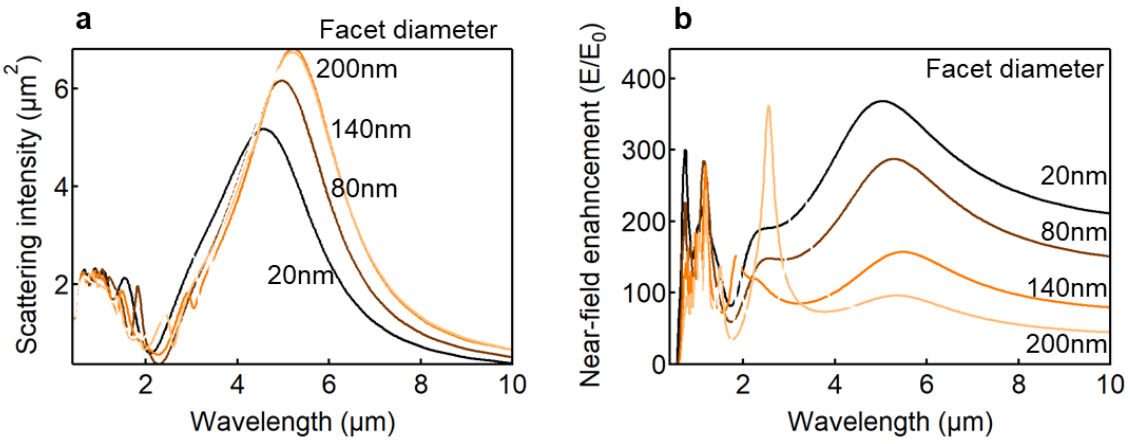

Figure S4: Effect of microsphere faceting in MSoF cavities. (**a-c**) Scattering cross-section and near-field enhancements for MSoF cavities by changing the facet width to 20nm to 200nm.

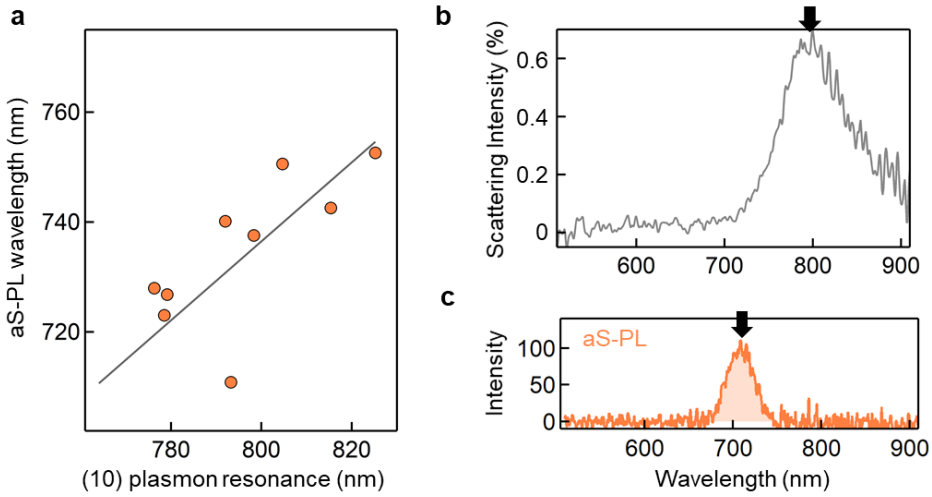

Figure S5: MIR-VAL correlated to plasmon resonance peak. (**a**) Peak aS-PL wavelength (when pumped at 785nm) for 9 NPoFs compared to their plasmon resonance positions. (**b**) Scattering spectrum from an individual NPoF cavity compared to (**c**) its aS-PL spectrum. Plasmon resonance of dominant (10) mode and aS-PL peak indicated by arrows.

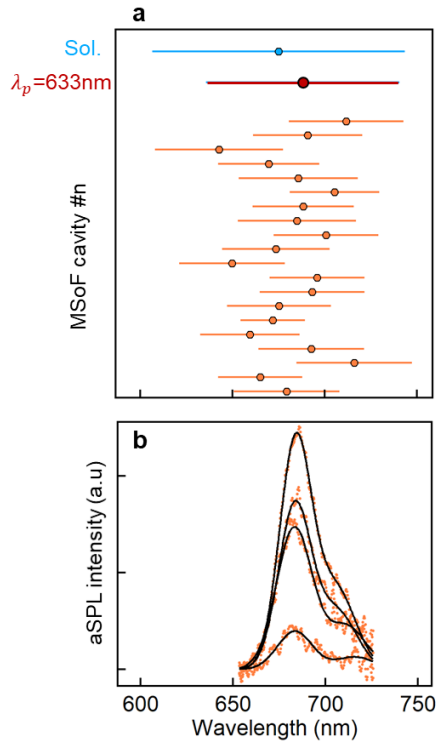

Figure S6: Spectral wandering of aS-PL. (**a**) Extracted peak positions of aS-PL spectra from different MSoF cavities, compared with PL spectra from direct pumping (red) and molecules in solution (blue). Horizontal lines indicate peak widths (FWHM). (**b**) Time dynamics of aS-PL spectra extracted at different time points from Figure 4a.

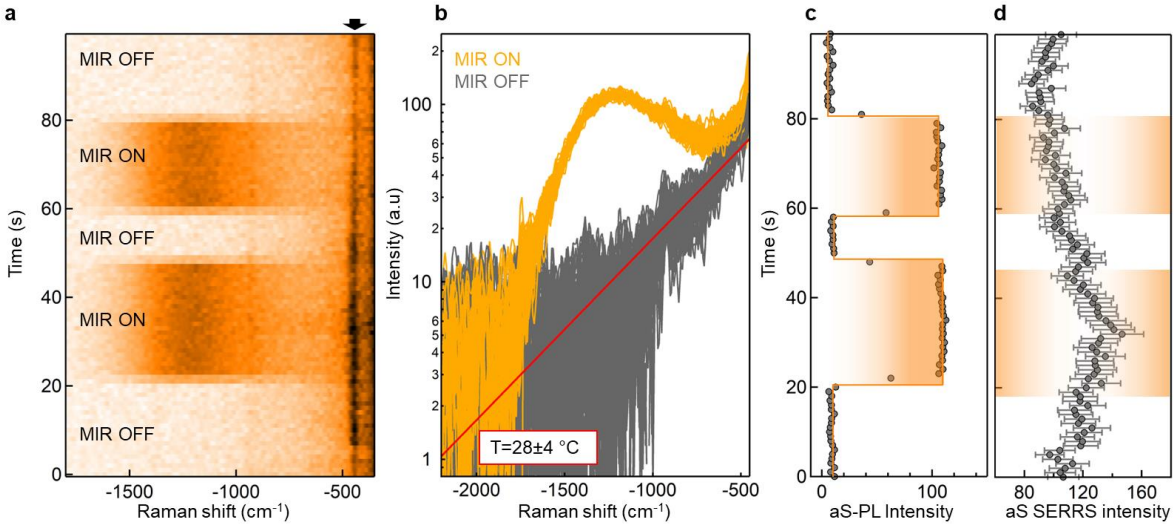

Figure S7: Estimating the effect of temperature on MIR-VAL. (**a**) Time series scan of anti-Stokes emission showing modulation of aS-PL intensity when switching MIR beam on/off. (**b**) Extracted anti-Stokes emission spectra from (a), both with (orange) and without (grey) MIR light (intensity on log scale). Red line is fit to inelastic scattering from free electrons in metal, extracted temperature labelled in bottom corner. (**c**) Integrated intensity of background from -800 to -1500cm^{-1}, while (**d**) SERRS intensity at 443cm^{-1} (top arrow in (a)) shows no modulation.

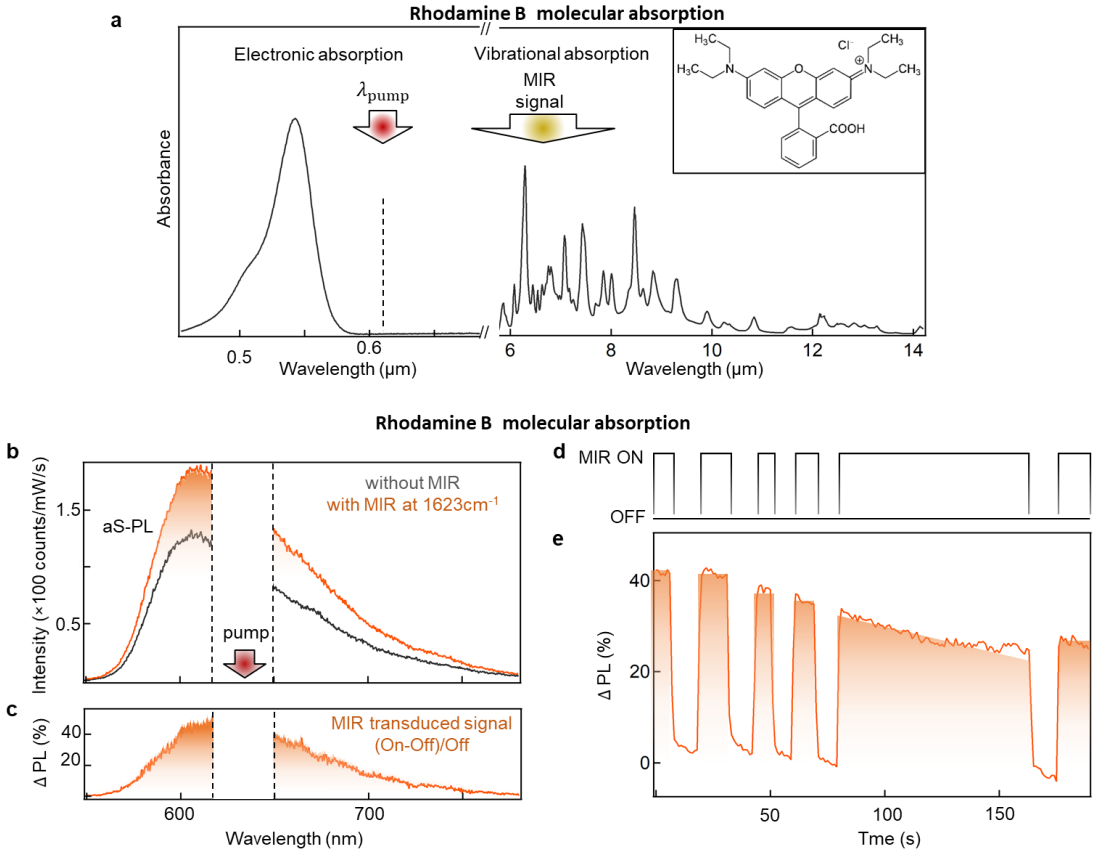

Figure S8: Detecting MIR-VAL in rhodamine B (RhB) molecules. (**a**) Electronic and vibrational absorption spectra of RhB molecules in solution. Arrows indicate NIR and MIR tuning. Inset shows the chemical structure of RhB. The assembly of RhB into the MSoF cavity is obtained using supramolecular assembly inside a cucurbit[7]uril (CB[7]) host molecule. (**b**) Stokes and anti-Stokes emission from pump ($\lambda_{\mathrm{pump}} = 633\mathrm{nm}$), with (orange) and without (grey) MIR light of average power 0.5μW/μm^2 on a single MSoF cavity. (**c**) Percentage difference in emitted signal transducted by MIR. (**d,e**) Modulation of (e) aS-PL intensity while switching the (d) MIR beam on and off.

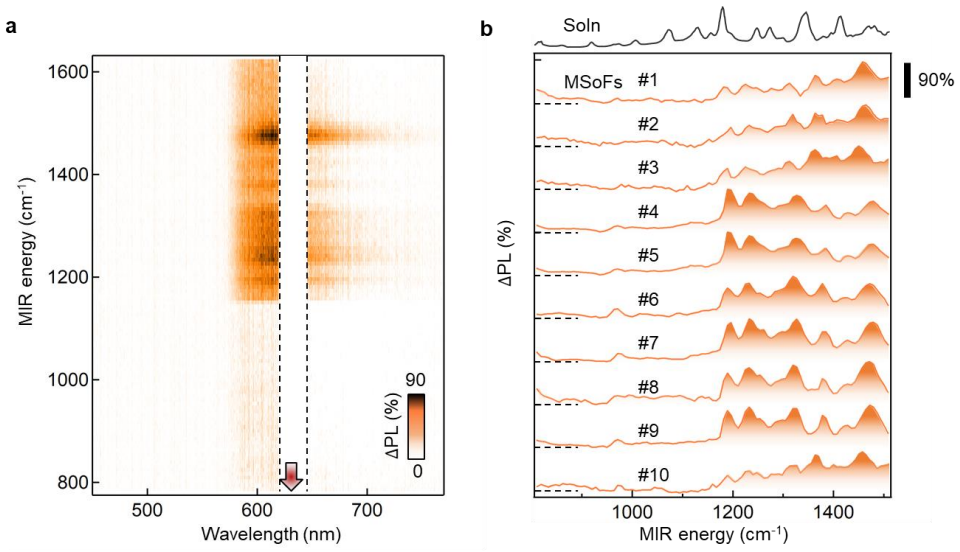

Figure S9: MIR spectrally-tuned vibrationally-assisted luminescence for RhB. (**a**) aS-PL intensity when tuning MIR energy on a single MSoF nanocavity. (**b**) Series of MIR-VAL spectra obtained for different MSoF cavities (#1 to #10) and compared to FTIR measurements of RhB in solution (solid grey line, top).

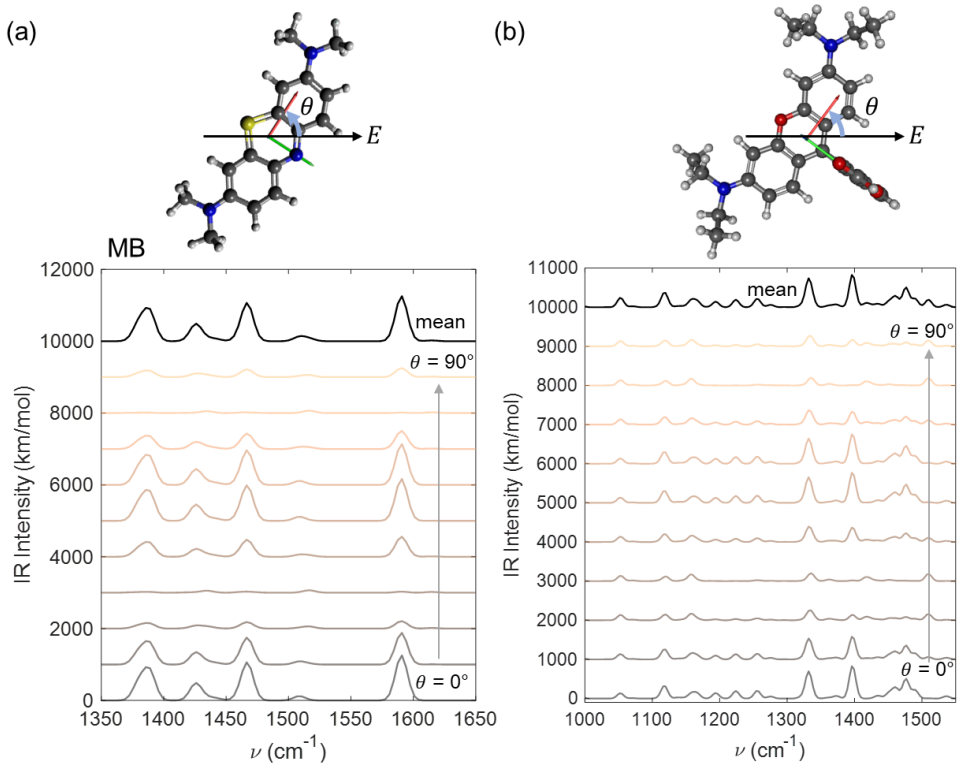

Figure S10: Influence of local optical E field under nanocavity. Angle-dependent IR spectrum of (**a**) MB and (**b**) RhB. Angle θ between parallel (θ = 0°) and perpendicular (θ = 90°) orientation to local E field. Different bands experience different enhancements and suppression of relative and overall intensities.

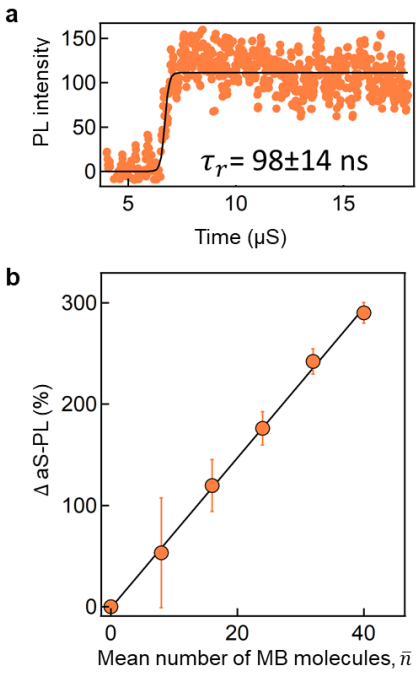

Figure S11: Temporal and spatial coherence of MIR-VAL. (**a**) Measured rise of aS-PL intensity on illuminating the individual MSoF cavity with QCL laser pulses, using single-photon detection. The experimental data is fit with a sigmodal curve to extract the rise time (τ_r). (**b**) Variation in aS-PL intensity when varying the mean number of MB molecules in individual MSoF cavities, across different samples. Error bars show standard deviation of as-PL on >10 MSoFs.

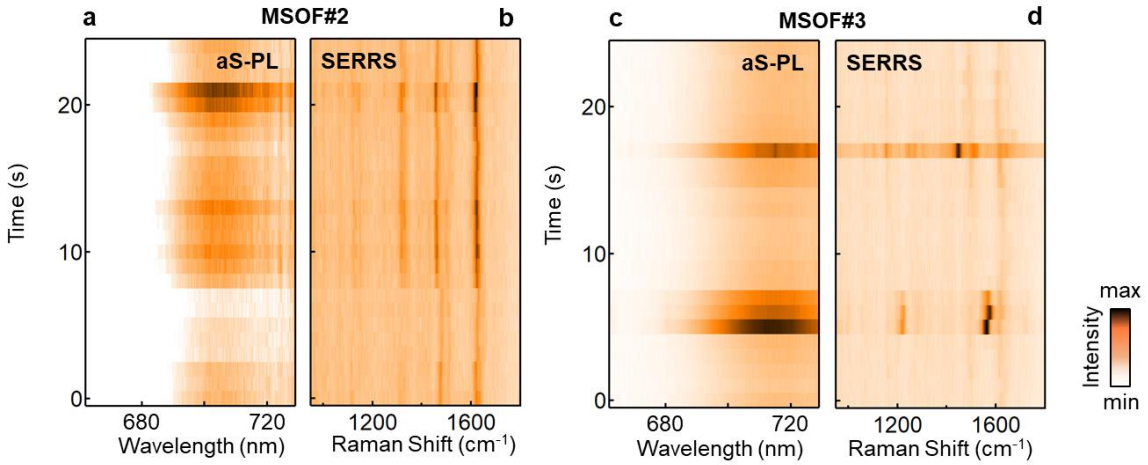

Figure S12: Single-molecule dynamics of MIR-VAL signal. Time dynamics of (**a,c**) aS-PL and (**b,d**) SERRS spectra form two different MSoF cavity with 0.7mW/μm^2 pump. Each spectrum is integrated for 1s.

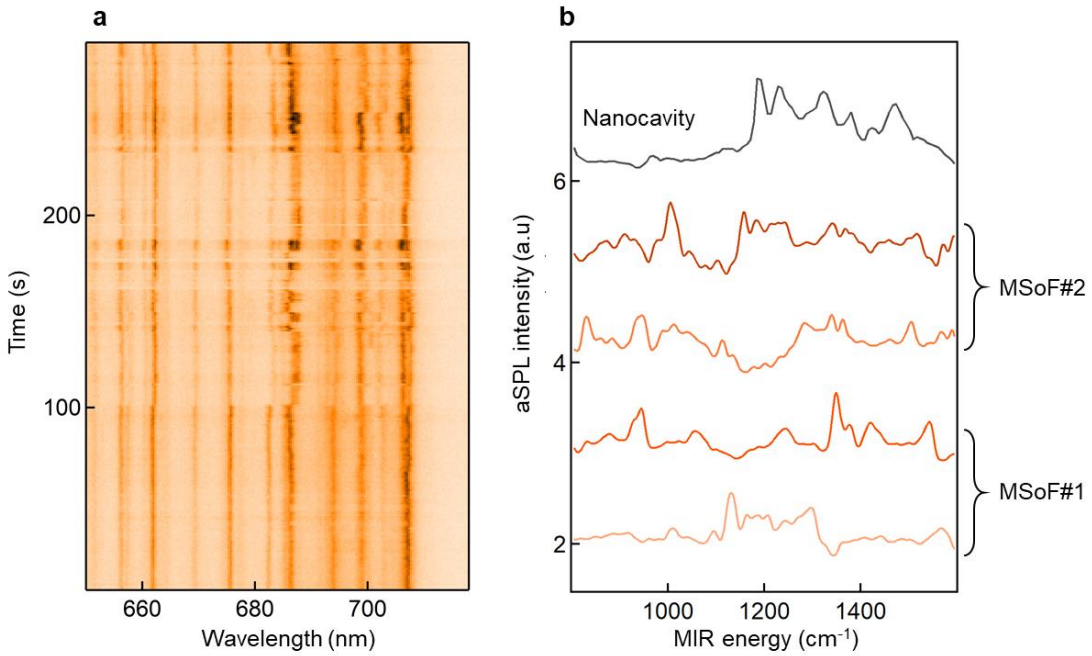

Figure S13: Single-molecule MIR-VAL spectroscopy. (**a**) Time-series SERRS of RhB molecules, exhibiting a long-lived picocavity >60s, using pump at 633nm, 50μW/μm^2. (**b**) Intensity of aS-PL when fast-tuning the MIR photon energy during a long-lived picocavity event. Two different scans collected from two different MSoF cavities within single picocavity events show changes in vibrational states that contribute most strongly to the MIRVAL signal.

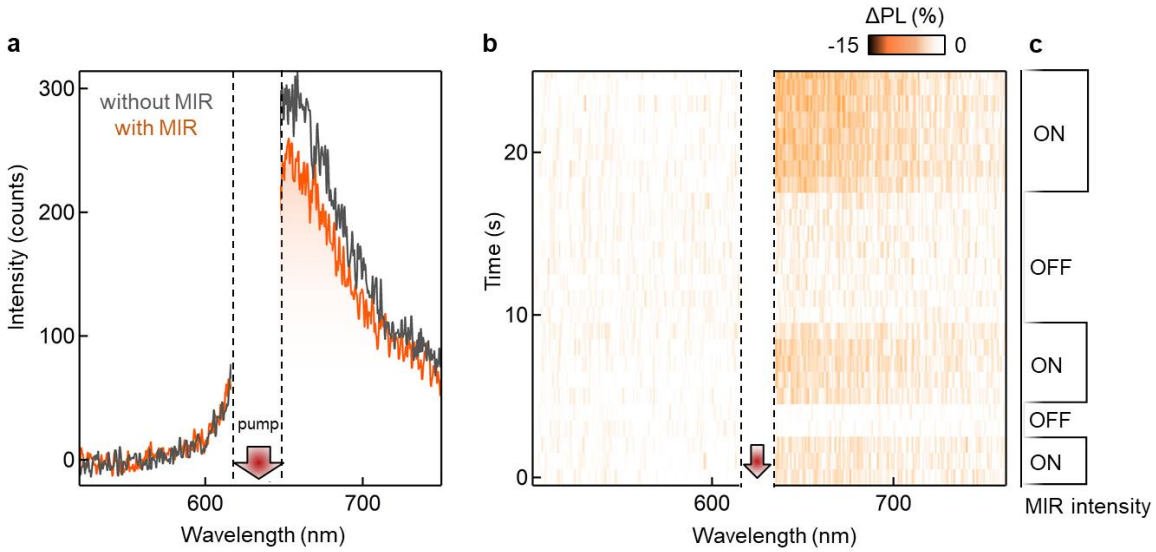

Figure S14: Modulation of PL outside the nanocavity systems. (**a**) Stokes and anti-Stokes emission from pump ($\lambda_{\mathrm{pump}} = 633\mathrm{nm}$), with (orange) and without (grey) MIR light on a RhB powder (large number of molecules) outside the nanocavity and on CaF_2 substrates. (**b**) Modulation of percentage change in emitted signal transduced by MIR, while switching the (**c**) MIR beam on and off. Note that Stokes emission

intensity decreases in the presence of MIR light and no change in the aS intensity, in contrast to positive change in the aS-PL in MSoF cavities.

Section S2: Rate Equation Model

The population dynamics of the MIR-VAL process is modelled using rate equations involving four states (Eqs.S1-S4), as shown in Fig.S6 (and Fig.1b in the main text). The ground state $|0\rangle$ population N_0 is coherently driven to the first vibrational state $|1_a\rangle$ by MIR light tuned to their energy difference. The population (N_{1a}) of $|1_a\rangle$ is defined by the rate of MIR light absorption, which in turn depends on the MIR photon flux (ϕ_{MIR}) and absorption cross-section (σ_{MIR}). This σ_{MIR} is modified by the presence of the nanocavity, which is accounted for by the near-field intensity enhancement $(E^2/E_0^2)_{MIR}$ estimated from full-wave simulations (Fig.1f). The vibrationally populated states relax back to $|0\rangle$ at rates which are well characterised and ~1ps for these molecules at room temperature [14,15 in main text]. The proximity of metals is known to speed up vibrational relaxation but remains on the ps scale.

The transition from $|0\rangle$ to $|0'\rangle$ is similarly driven by the pump beam, with population dynamics at state $|0'\rangle$ (coherent population $N_0'^{c}$) governed by the pump flux (ϕ_{pump}), cross-section at pump wavelength (σ_{pump}), as well as its near-field intensity enhancement $(E^2/E_0^2)_{\mathrm{pump}}$. In all dye molecules, there is then rapid small-energy relaxation from the initially electronically-excited state due to intramolecular rotations and vibrations (ivr). This population N_0^c thus loses its coherence, relaxing to the slightly lower energy state $|0'\rangle$ at rate γ_{ivr} which is on the order of (100fs)$^{-1}$. The vibrationally relaxed state (N_0') ultimately emits aS-PL to radiative relax back to $|0\rangle$. This rate of relaxation from $|0'\rangle$ to $|0\rangle$ (γ_r) is enhanced by the Purcell factor (P) of the nanocavity. The estimated values of pumping, Purcell and decay rates are tabulated in Fig. S6c. The optical cross-section of electronic and vibrational transitions of molecule outside the nanocavity are σ_{Pump}=10^{-3}nm^2 and σ_{MIR}=10^{-5}nm^2, respectively. The rate equations then follow:

$$\frac{\partial N_0}{\partial t} = -\phi_{MIR}\,\sigma_{MIR}\left(\frac{E^2}{E_0^2}\right)_{MIR}(N_0 - N_{1a}) + N_{1a}/\gamma_v + N_0'/(P.\gamma_r) \tag{S1}$$

$$\frac{\partial N_{1a}}{\partial t} = \phi_{MIR}\,\sigma_{MIR}\left(\frac{E^2}{E_0^2}\right)_{MIR}(N_0 - N_{1a}) - \phi_{\mathrm{pump}}\sigma_{\mathrm{pump}}\left(\frac{E^2}{E_0^2}\right)_{\mathrm{pump}}(N_{1a} - N_0^c) - N_{1a}/\gamma_v \tag{S2}$$

$$\frac{\partial N_0^c}{\partial t} = \phi_{\mathrm{pump}}\sigma_{\mathrm{pump}}\left(\frac{E^2}{E_0^2}\right)_{\mathrm{pump}}(N_{1a} - N_0^c) - \frac{N_0^c}{\gamma_{ivr}} \tag{S3}$$

$$\frac{\partial N_0'}{\partial t} = \frac{N_0^c}{\gamma_{ivr}} - \frac{N_0'}{P.\ \gamma_r} \tag{S4}$$

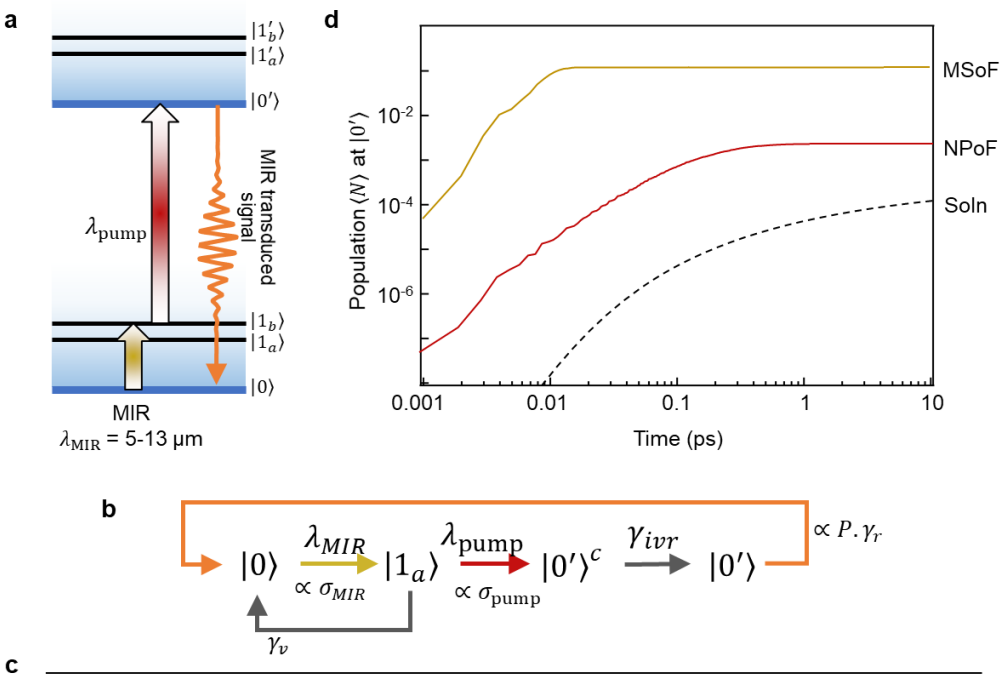

c

	$\left(\frac{E^2}{E_0^2}\right)_{MIR}\sigma_{MIR}$ (nm^2)	$\left(\frac{E^2}{E_0^2}\right)_{\text{pump}}\sigma_{pump}$ (nm^2)	$1/\gamma_v$ (ps)	$1/\gamma_{ivr}$ (ps)	$1/(P.\gamma_r)$ (ps)
Solution	10^{-5}	10^{-3}	1..0	0.1	1000
MSoF	$10^5\times10^{-5}$	$10^4\times10^{-3}$	1.0	0.1	10
NPoF	$10^2\times10^{-5}$	$10^5\times10^{-3}$	1.0	0.1	1.0

Figure S15: Temporal dynamics of MIR-VAL. (**a**) Energy diagram of electronic and vibrational levels of molecular dyes involved in the MIR-VAL process. (**b**) Modelling of energy states as a four-level system with rates of transition governed by differential equations described in the text. (**c**) Table of parameters used to describe the transitions. (**d**) Estimated population $\langle N_0^{'} \rangle$ at $|0'\rangle$ involved in aS-PL emission for the different nanocavity systems studied.

Section S3: Measurement of MIR-VAL efficiency

To estimate the MIR transduction efficiency, we directly compare the integrated aS-PL counts with the number of MIR photons illuminated on the sample.

Number of MIR photons illuminated is n_{MIR}=$P_{MIR} \times \lambda_{\text{MIR}}/hc$, where P_{MIR} is the MIR power/second, h is the Planck's constant and c is the speed of light. The estimated n_{MIR} with 1mW of average power at λ_{MIR}=6.3μm is 3.2×10^{16}. However, the large fraction of MIR light is reflected from the foil and the estimated transmission for 10nm Au foil is 10^{-4}. Therefore, the illuminated number of photons on a MSoF cavity is 3.2×10^{12}.

We calibrate the detection efficiency of our system at the λ_{pump} my measuring the reflected light from the Au foil beside the MSoF cavity. After accounting for the losses due to objective lens, beam splitters

(90:10 and 30:70), mirrors (7) and monochromator, the efficiency of detection is ~10%. Note that not all the light scattered from the MSoF cavity is collected by the objective lens. The nanocavity system is known to emit as a vertical dipole with angular cone larger than the NA of collection lens which limits the collection efficiency to 10^{-2}.

The measured aS-PL counts at 1mW of MIR power is 3×10^4 (Fig. 3b), so the end-to-end MIR transduction is 10^{-6}.

Importantly, λ_{pump} used to transduce the MIR signal is not operating near the saturation limit of molecular light emission indicating that higher pump powers improve the transduction efficiency.

To directly measure the transduction efficiency, we compare it with the molecular PL intensity by directly pumping the same MSoF cavity using the same collection system (Fig.2e). This is achieved by tuning the λ_{pump}=633nm to drive the $|0\rangle \rightarrow |0'\rangle$ transition without MIR light. The light emission from MSoF cavity at λ_{PUMP}=633nm is compared with $\lambda_{\mathrm{pump=750nm}} + \lambda_{\mathrm{MIR}}$ at the same power density. This way we estimate the efficiency of MIR-VAL to be >10%.